A Single-Cell Atlas of Tumor-Infiltrating Immune Cells in Pancreatic Ductal Adenocarcinoma

Authors
Hao Wang, Lu Chen, Lisha Qi, Na Jiang, Zhibin Zhang, Hua Guo, Tianqiang Song, Jun Li, Hongle Li, Ning Zhang, and Ruibing Chen

Correspondence
zhangning@bjmu.edu.cn;
rbchen@tju.edu.cn

Graphical Abstract

In Brief
Here, we employed mass cytometry to characterize the immune composition of PDAC microenvironment. We identified cell clusters with aberrant frequencies in tumors and observed elevated levels of immune markers, for example, PD-1, CD137L, and CD69. Moreover, TCGA PDAC tumors were stratified into three immune subtypes with different prognosis and distinct mechanisms of immune exclusion. Taken together, the data depicted a cell atlas of PDAC immune microenvironment and revealed useful cell phenotypes and targets for immunotherapy development.
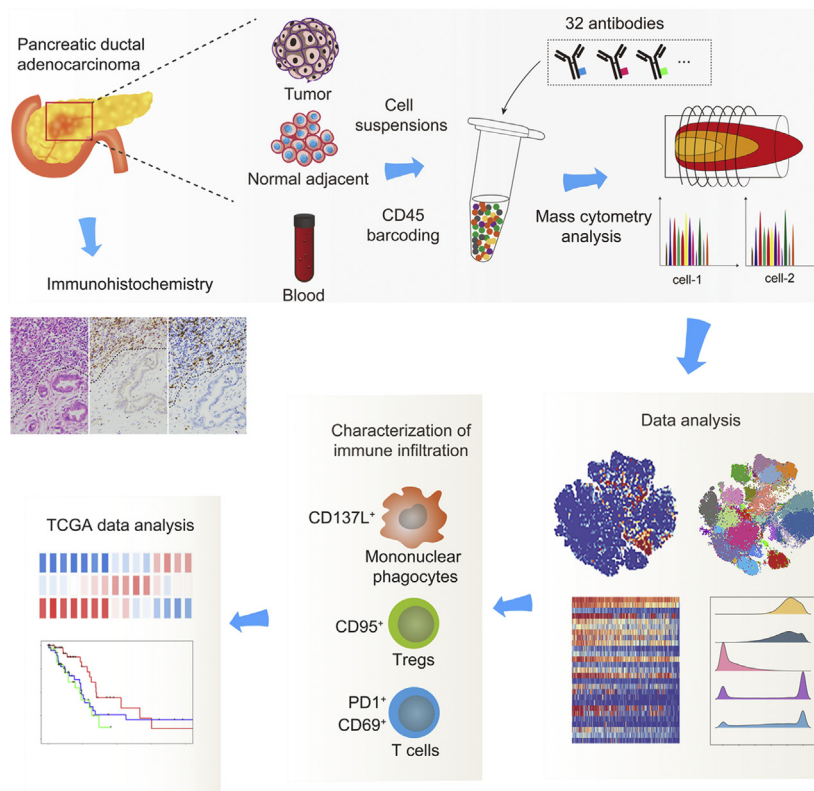
Highlights

- Mass cytometry characterized the immune composition of PDAC microenvironment.
- We identified 23 T-cell phenotypes with some exhibiting aberrant frequencies.
- PD-1 was extensively expressed in T cells.
- We observed elevated levels of functional markers, for example, CD137L and CD69.
- TCGA data analysis revealed distinct molecular mechanisms of immune exclusion.

A Single-Cell Atlas of Tumor-Infiltrating Immune Cells in Pancreatic Ductal Adenocarcinoma

Hao Wang[1,2,‡], Lu Chen[3,‡], Lisha Qi[3], Na Jiang[1], Zhibin Zhang[4], Hua Guo[3], Tianqiang Song[3], Jun Li[5], Hongle Li[5], Ning Zhang[3,6,*], and Ruibing Chen[1,*]

Pancreatic ductal adenocarcinoma (PDAC) is one of the most lethal malignancies with limited treatment options. To guide the design of more effective immunotherapy strategies, mass cytometry was employed to characterize the cellular composition of the PDAC-infiltrating immune cells. The expression of 33 protein markers was examined at the single-cell level in more than two million immune cells from four types of clinical samples, including PDAC tumors, normal pancreatic tissues, chronic pancreatitis tissues, and peripheral blood. Based on the analyses, we identified 23 distinct T-cell phenotypes, with some cell clusters exhibiting aberrant frequencies in the tumors. Programmed cell death protein 1 (PD-1) was extensively expressed in CD4^{+} and CD8^{+} T cells and coexpressed with both stimulatory and inhibitory immune markers. In addition, we observed elevated levels of functional markers, such as CD137L and CD69, in PDAC-infiltrating immune cells. Moreover, the combination of PD-1 and CD8 was used to stratify PDAC tumors from The Cancer Genome Atlas database into three immune subtypes, with S1 (PD-1^{+}CD8^{+}) exhibiting the best prognosis. Further analysis suggested distinct molecular mechanisms for immune exclusion in different subtypes. Taken together, the single-cell protein expression data depicted a detailed cell atlas of the PDAC-infiltrating immune cells and revealed clinically relevant information regarding useful cell phenotypes and targets for immunotherapy development.

Pancreatic ductal adenocarcinoma (PDAC) is a highly lethal disease with a 5-year survival rate of 7% (1). PDAC is currently the third leading cause of cancer-related mortality and predicted to be the second by the year of 2030 (2). Most patients with PDAC are diagnosed with unresectable or metastatic disease. Despite achieving a better understanding of the genomic nature of PDAC in the past decade (3–5), effective therapies, especially for the advanced disease, are still lacking.

PDAC neoplasms are characterized by a prominent desmoplastic reaction with a dense fibrotic stroma (1, 6). Extracellular matrix (ECM) components and nonneoplastic cells, including fibroblastic, vascular, and immune cells, occupy the majority of the tumor mass and form a complex and dynamic tumor microenvironment (TME) (1, 7). Desmoplasia is considered the biophysical barrier for T-cell infiltration (8, 9). However, a recent study indicates that stromal markers do not correlate with a paucity in T-cell accumulation, suggesting that the interaction between desmoplasia and the immune landscape in PDAC is more complex than previously recognized (10). T cells are the dominant immune cell types in the TME of PDAC (11, 12). High levels of CD4^{+} and CD8^{+} T cells in the tumor nests (Tn) and the proximity of cytotoxic T cells to cancer cells are both associated with prolonged survival (10, 11). Furthermore, increasing evidence has demonstrated the intertumoral and intratumoral heterogeneity of the infiltrating T lymphocyte subpopulations (10, 13). However, a detailed understanding of the immune composition of PDAC is still lacking.

Substantial evidence indicates that the function of PDAC-infiltrating T cells is attenuated by immune-suppressive cells, such as CD4^{+} forkhead box P3 (FoxP3)[+] regulatory T cells (Treg), M2 tumor-associated macrophages, and myeloid-derived suppressor cells (9, 14–16). Moreover, immune checkpoints are expressed in "exhausted" T cells in response to chronic antigen exposure and suppress the antitumor effects. Inhibiting these immune checkpoints can reactivate T cells to eliminate cancer cells. Immune checkpoint blockade, for example, anti–programmed cell death protein 1 (PD-1)/programmed cell death receptor ligand 1 and anti–cytotoxic T

From the [1]School of Pharmaceutical Science and Technology, Tianjin University, Tianjin, China; [2]Department of Clinical Laboratory, Affiliated Cancer Hospital of Zhengzhou University & Henan Cancer Hospital, Zhengzhou, China; [3]Tianjin Medical University Cancer Institute and Hospital, National Clinical Research Center for Cancer, Key Laboratory of Cancer Prevention and Therapy, Tianjin Medical University, Tianjin, China; [4]Department of General Surgery, Tianjin First Central Hospital, Tianjin, China; [5]Department of Molecular Pathology, Clinical Pathology Center, The Affiliated Cancer Hospital of Zhengzhou University & Henan Cancer Hospital, Zhengzhou, China; [6]Peking University First Hospital, Peking University Health Science Center, Beijing, China

[‡]These authors contributed equally to this work.

[*]For correspondence: Ruibing Chen, rbchen@tju.edu.cn; Ning Zhang, zhangning@bjmu.edu.cn.

lymphocyte (CTL)–associated protein 4 (CTLA-4), has gained remarkable successes in some cancers, such as melanoma and lung cancer (17, 18). However, single-agent immune checkpoint inhibitors for the treatment of PDAC have been disappointing to date (19, 20), likely because of the highly immunosuppressive TME, low infiltration, and recognition by effector T cells caused by low neoantigen burden in PDAC (21–23). Therefore, combination strategies that can completely activate antitumor T-cell responses are urgently needed. The exploration of the complex and heterogeneous immune landscape may provide insights for developing multiagent immunotherapies with improved antitumor efficacy.

To gain an in-depth understanding of the immune context-ure of PDAC, especially the T-cell compartment, we conducted immunohistochemistry (IHC) and single-cell mass cytometry analyses on specimens from 14 patients, including 12 PDAC patients and two patients diagnosed with chronic pancreatitis (CP). First, the level and localization of tumor-infiltrating T cells in the 14 collected tissue samples were examined with IHC. Next, mass cytometry was employed to analyze the expression of 33 immune markers in cells from the collected specimens. All collected samples were examined by IHC; however, few cells were obtained from PDAC tumors P11–P14 because of the low level of immune infiltration and/or the small size of these tissues; therefore, these four tumors were not used for mass cytometry analysis. In total, we were able to detect more than two million immune cells in 21 samples from ten patients, including eight treatment-naïve PDAC tumor samples, two CP tissues, nine peripheral blood mononuclear cell (PBMC) samples, a normal adjacent (Nadj) tissue from a CP patient, and a Nadj tissue from a PDAC patient (supplemental Table S1). The collected data were used to investigate the immune composition in the TME of PDAC, and the correlation between immune checkpoint molecules and other immune markers in single cells was also investi-gated. To further understand the immune landscape of PDAC in a larger patient population, we exploited the transcriptomic data of PDAC tumors from The Cancer Genome Atlas (TCGA), and the results showed that immune infiltration was highly relevant to the prognosis of PDAC, and different mechanisms were involved for immune exclusion in different immune sub-types of patients.

EXPERIMENTAL PROCEDURES
Clinical Samples

Surgical specimens from 12 treatment-naïve PDAC patients and two patients with CP were obtained from Tianjin Medical University Cancer Institute and Hospital. The CP samples were used as a non-tumorigenic pancreatic tissue reference to provide information regarding the differential pathological roles of tissue-resident immune cells. Whole blood samples were collected into sodium heparin tubes, and PBMCs were obtained by gradient centrifugation. PBMCs could represent the immune background of the patients and were employed as the control in the mass cytometry analysis. Given that the major

portion of the specimens was needed for pathological examination, we were only able to collect Nadj pancreatic tissues from two patients. Tumor grades were histologically determined by an experienced pathologist (supplemental Table S1). The studies in this work abide by the Declaration of Helsinki principles. All protocols were reviewed and approved by the Medical Ethics Committee at the Tianjin Medical University Cancer Institute and Hospital (bc2020049).

Antibodies

The antibodies (Abs) used for IHC staining were as follows: anti-CD3 (catalog no.: ab5690; Abcam), anti-CD8 (catalog no.: ZA-0508; ZSBio), and anti-rabbit immunoglobulin G-horseradish peroxidase (catalog no.: PV-6001; ZSBio). Metal-conjugated Abs used for mass cytometry were purchased from Fluidigm or in house labeled (supplemental Table S2). Ab labeling was performed using the Max-PAR antibody conjugation kit (Fluidigm) according to manufacturer's instructions. The concentration of each Ab was assessed after metal conjugation using a Nanodrop (Thermo Scientific). Conjugated Abs were titrated for optimal concentration for use.

IHC Staining

IHC staining was performed as previously described (24). In brief, formalin-fixed paraffin-embedded tissue blocks were cut into 5-μm slides and placed in an oven at 65 °C for 2 h. Xylene and graded concentrations of ethanol were used for sequential washing of the sections. Endogenous peroxidase activity and nonspecific staining were blocked by 3% H_2O_2 for 15 min and 3% bovine serum albumin (Roche) for 1 h. Incubation with the primary Abs was performed at room temperature for 30 min and then at 4 °C overnight. Tissue samples were washed with PBS three times and stained with the secondary Ab (1:200 dilution) at 37 °C for 1 h and then visualized by 3,3-diaminobenzidine staining, counterstained with 10% Mayer's he-matoxylin solution, dehydrated, mounted, dried, and examined under microscope.

Immunohistochemical stainings were assessed by experienced gastrointestinal pathologists blinded to the clinical information. Immune cell scores were calculated by counting the positive cells of indicated markers at 200× magnification from representative areas of Nadj, tumor margin (Tm), Tn surroundings, and Tn. Immune cell enrichment areas were used to represent the overall immune infiltra-tion of the specimen. For specimens with multiple immune cell enrichment areas, immune cell scores were represented by the average value of the counts. Both intraepithelial and intrastromal immune cell infiltrates of the representative areas were included in cell count.

Single-Cell Suspension Preparation

Tissues collected in surgery were immediately placed in ice-cold Dulbecco's modified Eagle's medium containing 1% penicillin/strep-tomycin. Tissues were delivered to laboratory within half an hour and processed to single-cell suspensions using the Tumor Dissociation Kit (Miltenyi). Briefly, tissues were minced into small pieces with scissors (~1 mm), incubated for 60 min in the enzyme mixture, filtered through a 70-μm cell strainer (Miltenyi), and washed in PBS twice. Then, the cells were labeled with cisplatin (Fluidigm), fixed, and cryopreserved in 10% dimethyl sulfoxide for subsequent analysis.

Peripheral blood samples were collected in heparin-containing tubes, mixed 1:1 with PBS, layered over Histopaque-1077 (Sigma), and centrifuged at 400g for 30 min at 25 °C. PBMCs were isolated from the interface between the Histopaque and the plasma. The collected cells were washed twice with PBS and processed similarly as the tissue samples before cryopreservation.

Ab Staining

For each patient, cells from each tissue were labeled with a unique barcode by incubating with CD45 Abs conjugated to distinct metal isotopes before pooling. In detail, each cell sample was first incubated with Fc receptor blocking solution (BioLegend), labeled with CD45 Ab, and washed in cell stain buffer (Fluidigm) for three times. Then samples from each patient were pooled into one tube. Pooled samples were labeled with 27 cell surface and five intracellular markers according to manufacturer's instructions. Cells were washed twice in cell stain buffer and resuspended in 1 ml of nucleic acid Intercalator-Ir buffer (125 nM Intercalator-Ir in fix and perm buffer [Fluidigm]) overnight at 4 °C. Cells were then washed once in cell stain buffer, once in PBS, and twice in water and diluted to 0.5×10^6 cells ml^{-1} in H_2O containing 10% of EQ Four Element Calibration Beads (Fluidigm) for subsequent mass cytometry data acquisition.

Mass Cytometry Data Acquisition and Preprocessing

The samples were analyzed on a CyTOF2 mass cytometry (Fluidigm) equipped with a SuperSampler fluidics system (Victorian Airships) at an event rate of <500 events per second. After acquisition, data variability between samples was calibrated by bead-based normalization in the CyTOF software, and all data were collected as .fcs files. Then the .fcs files were loaded into FlowJo (version: v10, BD Biosciences) to deconvolute the CD45-based barcoding and gated to exclude residual normalization beads, debris, doublets, and cisplatin-positive dead cells. All data were imported to R (version: 3.5.3) using the flowCore (version: 2.0.0) R/Bioconductor package, and signal intensities for each channel were arcsinh transformed with a cofactor of 5 (x_transf = asinh [x/5]) for subsequent clustering and high-dimensional analyses.

Mass Cytometry Data Clustering and Statistical Analysis

To balance the number of cells in each sample, 40,000 cells were randomly selected from each sample, and all cells were included when less than 40,000 cells were detected. Barnes–Hut implementation of t-distributed stochastic neighbor embedding (tSNE) in Rtsne (version: 0.15) R package was used to visualize the high-dimensional data in two dimensions. Clustering analysis was conducted using the PhenoGraph algorithm with parameter k = 30 implemented in Rphenograph (version: 0.99.1) R package. To visualize the relative expression and define the positive status of each marker, the expression was normalized between 0 and 1 to the 99th percentile, and the top percentile was set to 1, and the positive cutoff of each marker was 0.6. tSNE plots and heatmaps were displayed using the ggplot2 (version: 3.3.0) and ComplexHeatmap (version: 2.4.2) R package. Relative difference of population frequency, correlation analysis between the expression of markers, and paired tests of marker expression in PD-1-positive and PD-1-negative cells were all performed in R (version: 3.5.3) and specified in the corresponding figure legends.

TCGA Data Analysis

RNA sequencing data and clinical information for 146 PDAC samples were obtained from TCGA using the TCGAbiolinks (version: 2.16.0) R/Bioconductor package. "Immune score," which represents the infiltration level of immune cells in the tumor sites of the TCGA-PDAC samples, was calculated using the ESTIMATE algorithm (https://bioinformatics.mdanderson.org/estimate/). Nonsynonymous mutation counts per Mb of the TCGA samples were analyzed using FireBrowse (http://firebrowse.org/), which provides access to analyze data obtained from TCGA. The stratification of the TCGA sample was conducted by two steps. First, we defined the "immune desert" subtype according to the minimum one-third "Immune score." Then, the remaining samples with PD-1 and CD8 greater than their 33rd

percentile are defined as the "CD8$^+$PD-1$^+$ immune" subtype, and the remainder of samples was allocated to the "CD8-PD-1-immune" subtype. Gene set variation analysis (GSVA) was performed to identify the pathway alterations across the three TCGA-PDAC subtypes using the R/Bioconductor package GSVA (version: 1.36.0). Gene sets for GSVA were obtained from the MSigDB database C2-canonical pathways (version: 7.1). The TCGA-PDAC gene expression matrix was subjected to the GSVA algorithm to calculate GSVA scores for each gene set with at least ten overlapping genes. The significance of the enrichment of the TCGA-PDAC subtypes was estimated using a simple linear model and moderated with the F-statistic by the R/Bioconductor package limma (version: 3.44.1). Log-rank tests and Kaplan–Meier survival curves were applied to compare the overall survival among the TCGA-PDAC subtypes using R package survival (version: 3.1.12) and survminer (version: 0.4.6).

Experimental Design and Statistical Rationale

The mass cytometry (CyTOF2) experiments were performed on single-cell suspensions obtained from eight treatment-naïve PDAC tumor samples, two CP tissues, nine PBMC samples, one Nadj tissue from a CP patient, and one Nadj tissue from a PDAC patient. Statistical analysis was conducted by using the Wilcoxon rank-sum test, and $p < 0.05$ was considered to be statistically significant. All statistical analyses were performed using R (version: 3.5.3).

RESULTS

Mass Cytometry Profiling of Tumor-Infiltrating Immune Cells in Pancreatic Samples

In this study, we collected freshly resected tissues from 12 treatment-naïve patients diagnosed with PDAC and two patients with CP (supplemental Table S1). The level of T lymphocyte infiltration in the collected tissues was first examined by IHC against both CD3 and CD8. We observed marked interpatient variability in the density of the infiltrated T cells, and tumors from several patients, for example, P11, P13, and P14, exhibited low T-cell numbers, consistent with a "cold tumor" phenotype (Fig. 1A, supplemental Fig. S1A). In addition, we observed a decreasing gradient of CD8$^+$ CTLs and total T-cell numbers across Tm, Tn surroundings, and Tn, showing an exclusion distribution pattern (Fig. 1A). Tumor tissues exhibited higher density of T cells, and even the Tn showed more abundant T cells compared with the Nadj tissues ($p < 0.01$, Fig. 1A). Moreover, the two CP tissues were enriched with T cells, exhibiting a comparable level of T-cell infiltration to the tumor samples (supplemental Table S3).

To further investigate the cellular composition of the infiltrated immune cells, we performed a multiscale mass cytometry analysis on the resected tissues and isolated PBMCs from these patients. To simultaneously analyze the immune compartments of the pathological tissues, the Nadj tissues, and the peripheral blood samples, we barcoded these three different types of samples with anti-CD45 Abs conjugated to distinct metal isotopes before the samples were pooled (25). Next, the pooled single-cell suspension samples were stained with additional 32 Abs and then analyzed by mass cytometry (Fig. 1B and supplemental Table S2). The Ab panel was designed to focus on the functional diversity of T
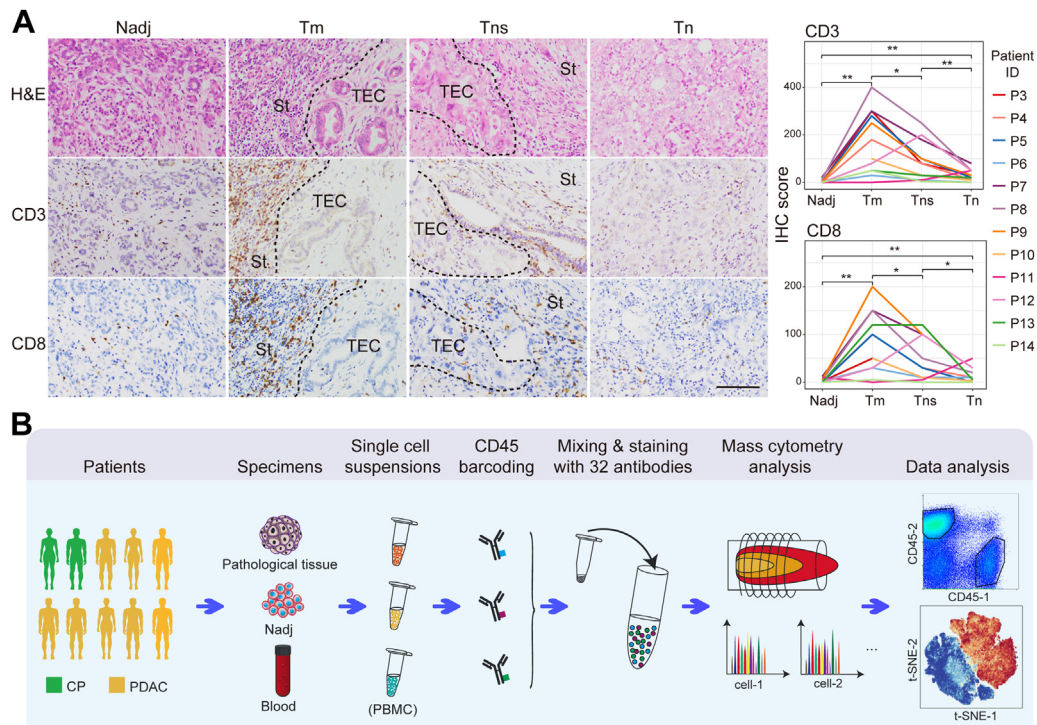
FIG. 1. **Investigation of the immune landscape of PDAC.** *A*, representative IHC images stained against CD3 and CD8 from different regions of a PDAC tumor (*left panel*; scale bar, 100 μm). Line graphs showing the T-cell density scores in tumors from all the enrolled PDAC patients. Paired Wilcoxon test was used for statistical analysis (*$p < 0.05$, **$p < 0.01$). *B*, workflow of the mass cytometry experiments. Different types of samples from one patient were stained with anti-CD45 conjugated with different isotopes and then combined for mass cytometry analysis. For PDAC tumors without paired Nadj or PBMC sample from the same patient, two anti-CD45 antibodies conjugated with different isotopes were employed for the barcoding. See also supplemental Figs. S1 and S2 and supplemental Tables S1–S3. IHC, immunohistochemistry; Nadj, normal adjacent tissue; PBMC, peripheral blood mononuclear cell; PDAC, pancreatic ductal adenocarcinoma; St, stroma; TEC, tumor epithelial cell nest; Tm, tumor margin; Tn, tumor nest; Tns, tumor nest surrounding.

cells. Given that a large portion of the specimens was reserved for pathological examination and few immune cells existed in the adjacent normal tissue, we were only able to obtain enough cells for the mass cytometry analysis from two normal tissues in this study, including one from a PDAC patient and one from a CP patient. In addition, few cells were obtained from PDAC patients P11–P14, therefore mass cytometry data were acquired only for two CP patients (P1 and P2) and eight PDAC patients (P3–P10). Of note, the data of Nadj and CP samples were included for reference; however, they should be treated with caution because of the small sample size. After debarcoding and quality control by manual gating strategy (supplemental Fig. S1*B*), we detected approximately 200,000 tumor-infiltrating immune cells and more than 1,800,000 PBMCs for the subsequent analysis (supplemental Fig. S1*C*). Multidimensional scaling analysis revealed significant inter-patient heterogeneity for both PDAC-infiltrating immune cells and PBMC samples, while the immune composition of the two CP samples was highly similar to each other (supplemental Fig. S1*D*). To address the discrepancies in total numbers of cells per sample, 40,000 cells were randomly selected from each sample for the downstream analysis, and all cells were included when less than 40,000 cells were detected.

Correlation analysis of marker frequencies showed that the randomly selected cells exhibited good consistency, suggesting that the random sampling could decently represent the whole sample (supplemental Fig. S1, *E* and *F*). Meanwhile, technical replicate analysis of a PBMC sample demonstrated high reproducibility of the mass cytometry experiments (supplemental Fig. S2).

The Single-Cell Immune Landscape of PDAC

To visualize the expression of markers in all the measured immune cells (CD45+), the dimensionality reduction algorithm tSNE (26, 27) was applied to generate two-dimensional graphs for each marker (Fig. 2*A* and supplemental Fig. S3*A*). The distribution of cells from individual samples in the tSNE plot was shown in supplemental Fig. S3*B*. To precisely map the diverse cell phenotypes, we employed the PhenoGraph clustering algorithm (28), which was widely used for the clustering of high-dimensional single-cell data, and identified 29 individual cell clusters (Fig. 2*B* and supplemental Fig. S3*C*). Marker expression profiles assigned these clusters to four main immune compartments, including T cells, B cells, NK cells, and mononuclear phagocytes (MPs) (Fig. 2, *C* and *D*, supplemental Fig. S3*D* and supplemental Table S4).
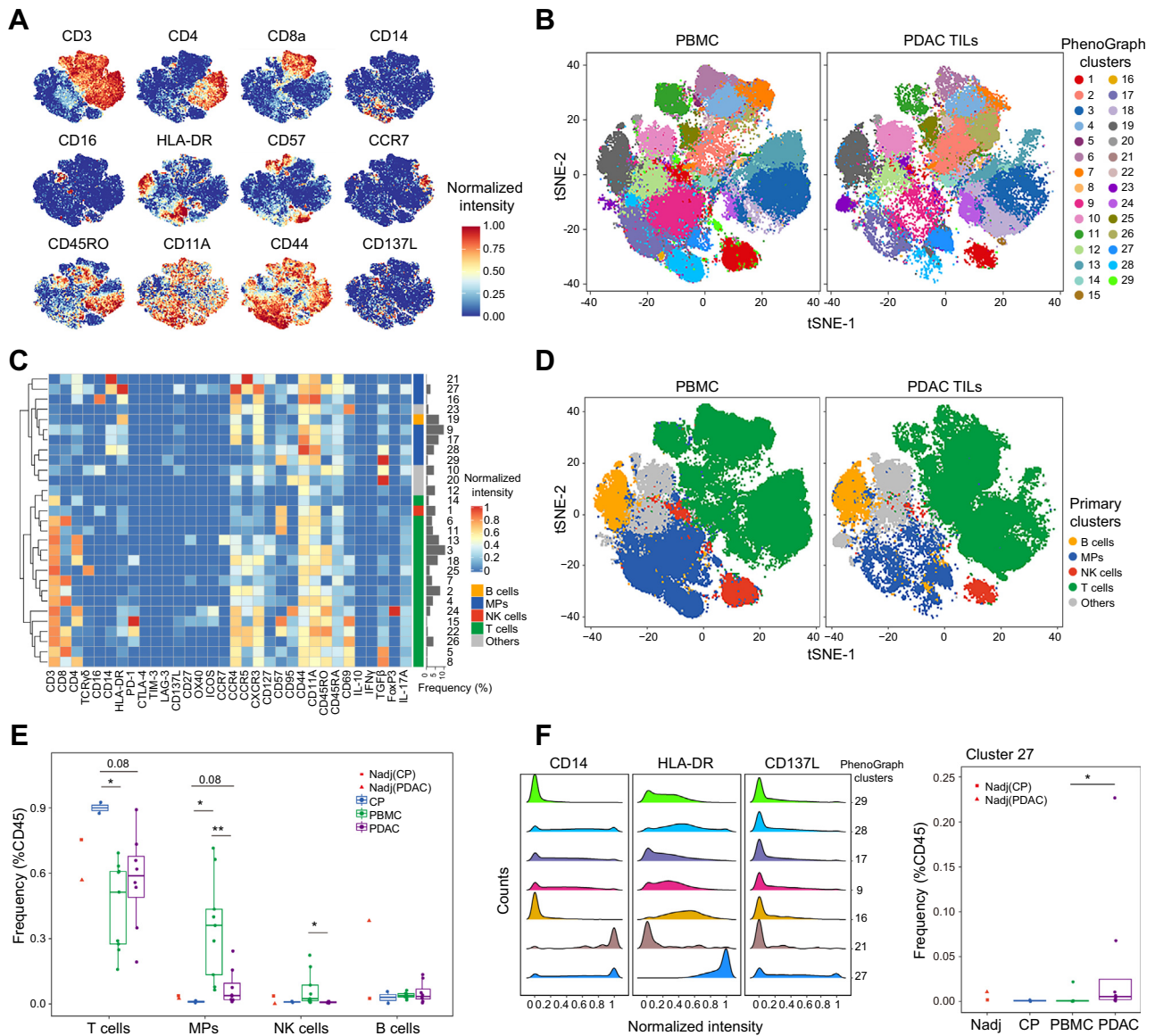
FIG. 2. **Identification of immune cell subtypes in the PDAC TME.** *A*, cells colored by normalized expression of indicated markers on the t-distributed stochastic neighbor embedding (tSNE) maps. *B*, tSNE plots of CD45$^+$ cells colored by PhenoGraph-identified clusters. *C*, heatmap showing the markers' expression of PhenoGraph-identified clusters. *D*, tSNE plots displaying cells of the main immune cell compartments based on the manual annotation of the PhenoGraph clusters. *E*, frequencies of the main immune cell compartments in Nadj, CP, PBMC, and PDAC samples. Boxplot center lines = median, lower bound = 25% quantile, upper bound = 75% quantile, lower whisker = the smallest observation greater than or equal to the lower hinge −1.5 × interquartile range (IQR), and upper whisker = the largest observation less than or equal to the upper hinge + 1.5 × IQR. Wilcoxon rank-sum test was used for statistical analysis (*$p < 0.05$). *F*, histograms showing the expression of indicated markers in PhenoGraph clusters of myeloid cells (*left*) and boxplot showing the frequencies of cluster 27 in different samples. Wilcoxon rank-sum test was used for statistical analysis (*$p < 0.05$). Statistical analysis was not performed on Nadj samples. See also supplemental Fig. S3, supplemental Tables S4 and S5. CP, chronic pancreatitis; MP, mononuclear phagocyte; Nadj, normal adjacent tissue; PBMC, peripheral blood mononuclear cell; PDAC, pancreatic ductal adenocarcinoma; TME, tumor microenvironment.

T cells were detected as the most abundant cell population in the PDAC TME with a mean frequency of 56% (Fig. 2*E*), consistent with previous reports (10, 11). The mean frequency of T cells in PBMCs (44%) was slightly lower compared with that in the tumors with large interpatient variability in both types of samples. Moreover, the mean percentage of T cells was considerably higher in the two CP samples (89%)

(Fig. 2*E*). It should be noted that different numbers of cells from individual samples were used for the analysis (supplemental Table S5).

Frequencies of the other immune cells were lower compared with T cells in PDAC. The mean frequency of NK cells was 0.8%, significantly lower compared with that in PBMC samples (6.6%) (Fig. 2*E*). We observed that the

frequency of CD95$^+$ NK cells in PDAC tumors was markedly higher compared with PBMCs (supplemental Fig. S3E). CD95 is a prototypic death receptor both in and outside the immune system (29). Our data suggested that the CD95-mediated apoptosis may contribute to the depletion of PDAC-infiltrating NK cells. B cells constituted approximately 5% of the detected immune cells in PDAC tumors, comparable to that in CP tissues and peripheral blood, and its frequency was higher in the adjacent normal tissues from one of the PDAC patients (Fig. 2E). Interestingly, we observed that the tumor-infiltrating B cells expressed higher levels of CC chemokine receptor 5 (CCR5) compared with B cells in PBMC samples (supplemental Fig. S3F). CCR5 is not expressed in normal B cells but has been associated with the migration and proliferation of pathological B cells (30, 31). The results indicated that CCR5 may play a role in regulating the infiltration and biological functions of B cells in the TME of PDAC.

The mean frequency of MPs in PDAC was 7.5%, with marked interpatient viability, ranging from 1.04% to 24.3% (Fig. 2E). The percentage of PDAC-infiltrating MPs was lower compared with T cells in majority of the investigated samples, which was consistent with observations in an earlier study (11). PhenoGraph clustering analysis revealed seven subpopulations of MPs in the analyzed samples, among which cluster 27 expressing CD14 and HLA-DR and partially expressing the 4-1BB ligand (CD137L) predominated the MP population in PDAC and exhibited an increased frequency compared with blood (Fig. 2F). Cells in cluster 27 also broadly expressed cytokines transforming growth factor beta and interleukin-17A (supplemental Fig. S3G). This phenotype showed great variability between patients. In one PDAC sample, cluster 27 constituted 22% of all immune cells, and its mean frequency was 4% among all eight samples. CD137L is expressed by antigen-presenting cells, and its interaction with its receptor delivers a potent active antitumor immune response in some cancers; therefore, its agonists are currently being exploited as potential immunotherapeutic reagents (32, 33). Our data suggested the potential therapeutic benefit to target CD137L in some PDAC patients.

The Heterogeneous Phenotypes of PDAC-Infiltrating T Cells

Next, we performed tSNE and PhenoGraph analyses focusing on T cells to exhaustively map the diverse T-cell phenotypes (Fig. 3, A and B). This approach led to the identification of 23 T-cell subsets, including ten CD4$^+$ subsets, nine CD8$^+$ subsets, and four double-negative subsets (Fig. 3, B and C). CD4$^+$ and CD8$^+$ T cells accounted for 50% and 46% of all T cells across tumors, respectively. No statistically significant difference was observed for the percentage of CD4$^+$ T cells among different types of specimens, and the two CP samples contained higher percentage of CD8$^+$ T cells compared with PBMCs (supplemental Fig. S4A). In addition, we found that the double-negative T cells accounted for 4% of

all T cells in PDAC tumors, which was slightly lower than that in PBMCs (supplemental Fig. S4A). The frequency of cluster T17 composed of γδ T cells was elevated in PDAC, but these cells accounted for a small proportion of the T compartment. Daley et al. (12) previously reported that the γδ T-cell population constituted ~40% of tumor-infiltrating T cells in PDAC; however, our data and several previous reports did not confirm their findings (10, 13).

To further explore T-cell subset diversity, we manually annotated the PhenoGraph clusters based on the expression of characteristic markers and defined eight major classes of T cells (Fig. 3, C–E and supplemental Fig. S4, B and C). Effector memory (EM) CD4$^+$ T cells (CD4$^+$ EM, CCR7^{low}CD45RO$^+$) accounted for 18% of T cells on average in PDAC tumors, lower compared with PBMCs (Fig. 3E and supplemental Fig. S4B). Five subsets of CD4$^+$ EM were identified, exhibiting great heterogeneity among physiological sample types (Fig. 3F). For example, subsets T6 and T8 were significantly more abundant in PBMCs compared with PDAC (Fig. 3F). Furthermore, the frequency of subset T23 with low expression of chemokine receptors and adhesion molecules was elevated in PDAC and CP samples (Fig. 3F and supplemental Fig. S4D). T23 cells may be in a quiescent and nonfunctional state given that chemokine receptors and adhesion molecules play key roles in lymphocyte trafficking and biological activities (34, 35). As expected, CD4$^+$ naïve cells (CCR7$^+$CD45RO^{low}) were rarely observed in the PDAC TME and the CP samples (Fig. 3E and supplemental Fig. S4B).

CD4$^+$ PD-1$^+$ T cells accounted for 20% of all T cells in PDAC. Greater than 40% of CD4$^+$ T cells were PD-1$^+$ in PDAC tumors, markedly higher compared with PBMCs (<1%) (Fig. 3E and supplemental Fig. S4B). All the analyzed PDAC samples exhibited high frequency of PD-1 in the CD4$^+$ population, ranging from 16% to 74% (Fig. 3, E and F). Cluster T14 was the major phenotype of the PD-1$^+$CD4$^+$ T-cell population in PDAC with significantly higher frequency compared with CP and blood samples (Fig. 3F). This broad expression of PD-1 in CD4$^+$ T cells was not observed in previous studies of lung, kidney, and breast cancers (25, 36, 37) and may represent a unique characteristic of PDAC.

Tregs (T19) were identified based on the expression of CD4$^+$, FoxP3$^+$, and CD127^{low} (Fig. 3C). Tregs were significantly enriched in PDAC TME compared with PBMC and CP samples with an average percentage of 9% across PDAC samples (Fig. 3E and supplemental Fig. S4B), which was consistent with previous reports (13, 14). In addition, we observed a lower percentage of Treg in CP samples compared with the PBMCs, suggesting an uncontrolled immune reaction in the inflamed tissues (Fig. 3E). Furthermore, Treg cells expressed higher levels of inhibitory checkpoint CTLA-4, costimulatory checkpoints inducible T-cell costimulatory (ICOS), and tumor necrosis factor receptor superfamily member 4 (OX40) compared with the other subsets of CD4$^+$ cells in PDAC (supplemental Fig. S4D).
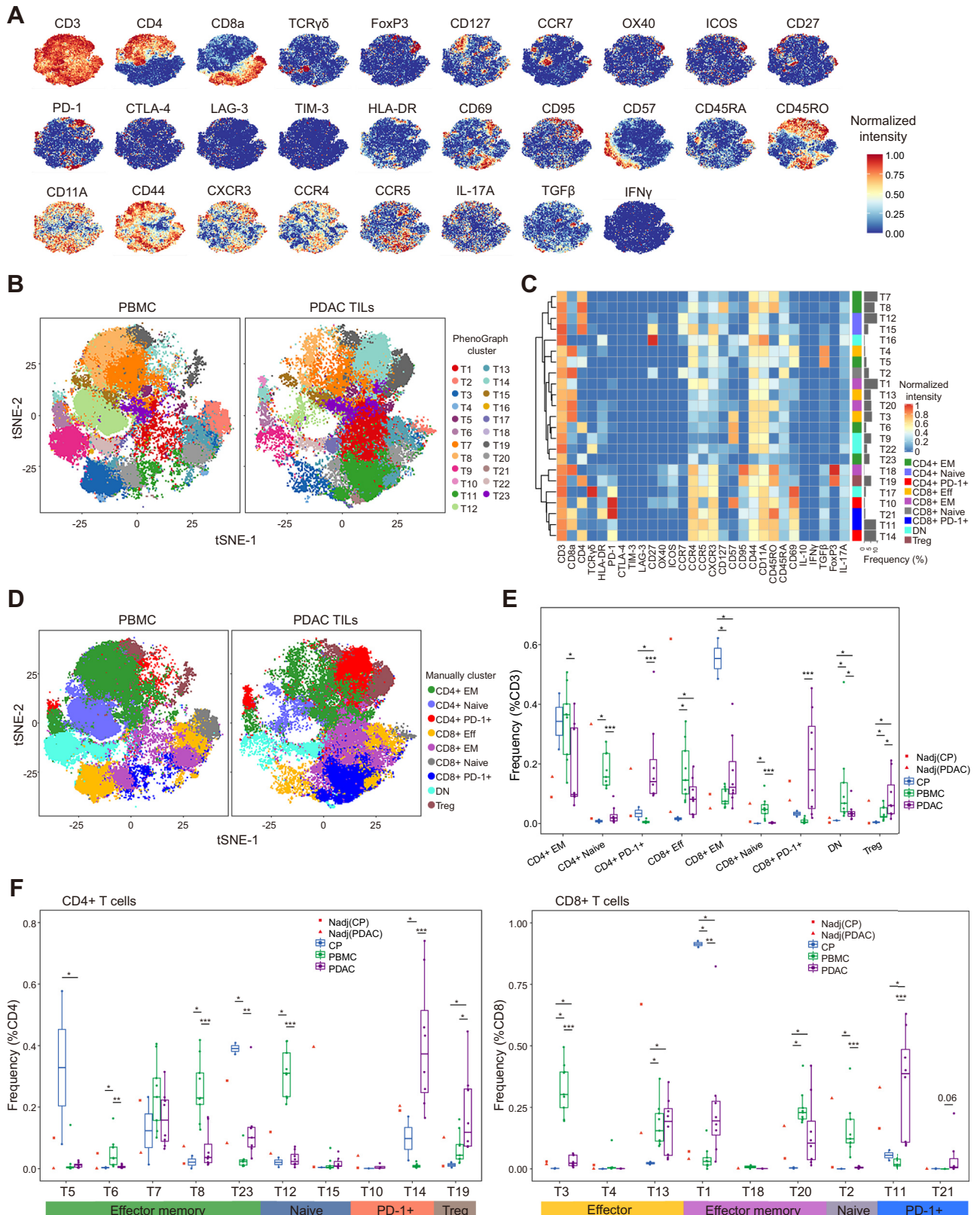
FIG. 3. **Characterization of infiltrating T cells in the PDAC TME.** *A*, tSNE plots of T cells colored by normalized expression of indicated markers. *B*, tSNE plots of T cells colored by PhenoGraph-identified clusters. *C*, heatmap showing the markers' expression in PhenoGraph-identified clusters of T cells. *D*, tSNE plots displaying T-cell subsets based on the manual annotation of the PhenoGraph clusters. *E*,

CD8$^+$ cells are the major immune cell compartment in TME that exhibit antitumor activity (38). Our data showed that CTLs in PDAC were mainly composed of three classes, including effector (CD8$^+$ Eff, CCR7^{low}CD45RA$^+$), EM (CD8$^+$ EM, CCR7^{low}CD45RO$^+$), and PD-1$^+$ phenotypes (Fig. 3E and supplemental Fig. S4B). CD8$^+$ naïve cells were rarely observed in PDAC samples, and the CD8$^+$ EM phenotype was the largest compartment of CTLs in PDAC with a mean frequency of 40%, followed by PD-1$^+$ cells with mean frequency of 38% (Fig. 3, E and F and supplemental Fig. S4B). Within the three observed CD8$^+$ EM subsets, cluster T1 with relatively lower CD44 expression compared with the other two CD8$^+$ EM clusters was significantly more abundant in PDAC compared with PBMCs and exhibited the highest frequency in the CP samples (Fig. 3F).

PD-1 was expressed in 38% CTLs in the PDAC tumors, indicating an exhausted status of PDAC-infiltrating CTLs (Fig. 3, E and F and supplemental Fig. S4B). Two PD-1$^+$ subsets were observed, including T11 with relatively lower PD-1 expression and T21 with higher PD-1 expression (Fig. 3F and supplemental Fig. S4D). T11 dominated the PD-1$^+$ CTL population with an increasing trend from PBMCs to tumor adjacent normal tissues followed by PDAC tumors, and the frequencies of PD-1$^+$ CTL greatly varied across tumors (Fig. 3F). PD-1 expression is a prerequisite for the clinical application of PD-1 blockade therapy (39, 40). The observed extensive expression of PD-1 in both CD4$^+$ and CD8$^+$ compartments suggested a potential benefit of blocking PD-1 for PDAC treatment, but the significant interpatient heterogeneity of PD-1$^+$ cells indicated the need for individualized treatment.

To investigate the heterogeneity of immune cell signatures across PDAC and PBMC samples, the frequencies of different T-cell subsets from individual patients were plotted, revealing increased variability across PDAC tumors compared with PBMC samples, especially for the CD8$^+$ T-cell clusters (supplemental Fig. S4E). Furthermore, the Kullback–Leibler divergence of individual sample composition relative to the mean composition was computed for the different T-cell compartments. The results showed that PDAC samples exhibited significantly increased divergence in CD8$^+$ T cells compared with PBMC samples (supplemental Fig. S4F).

The Expression of Immune Checkpoint Molecules on PDAC-Infiltrating T Cells

To further reveal the functional state of PDAC-infiltrating T cells at the single-cell level, we examined the expression of a group of functional markers, such as immune checkpoint molecules. Inhibitory checkpoint molecules are typically overexpressed in tumor-infiltrating lymphocytes and widely exploited as therapeutic targets in immunotherapies (41). Of the four examined inhibitory checkpoint molecules, PD-1 was the only molecule significantly overexpressed in PDAC-infiltrating T cells (Fig. 4, A and B and supplemental Fig. S5A). CTLA-4, T-cell immunoglobulin and mucin-domain containing-3 (TIM-3), and lymphocyte-activation gene 3 (LAG-3) all exhibited low expression on PDAC-infiltrating T cells in our data.

The expression of costimulatory checkpoint molecules, such as ICOS, CD27, and OX40, has not been previously studied in PDAC. Here, we found that these three costimulatory molecules were expressed in tumor-infiltrating T cells with mean frequencies of 10%, 5%, and 8% (Fig. 4A). The frequencies of ICOS and OX40 were slightly increased in PDAC compared with the CP and PBMC samples, but the difference was statistically insignificant. Interestingly, the proportion of OX40$^+$ cells in the CD4$^+$ compartment was significantly increased in PDAC tumors compared with PBMCs (supplemental Fig. S5A). Furthermore, we found that the expression of the major histocompatibility complex class II cell surface receptor HLA-DR, a marker of activated T cells (42), was significantly elevated in both CD4$^+$ and CD8$^+$ PDAC-infiltrating T cells compared with the other samples (Fig. 4A and supplemental Fig. S5A). Collectively, our data showed that the inhibitory checkpoints other than PD-1 were expressed at very low levels in PDAC-infiltrating immune cells, whereas some of the costimulatory molecules, such as OX40, were elevated.

The Expression of Functional Markers on PDAC-Infiltrating T Cells

Next, we examined the expression of several chemokine receptors, adhesion molecules, and other functional markers on T cells. Chemokine receptors CCR4, CCR5, and CXCR3 exhibited significantly increased expression on PDAC-infiltrating T cells compared with circulating T cells (Fig. 4C and supplemental Fig. S5B). Meanwhile, similar proportions of T cells positive for adhesion molecules CD11A (integrin alpha-L) and CD44 (CD44 antigen) were noted in PDAC tumors and PBMCs (Fig. 4C and supplemental Fig. S5B). In addition, the data showed that the percentage of CD57$^+$ CTLs in the PDAC TME was considerably reduced compared with blood (Fig. 4C and supplemental Fig. S5, B and C). CD57 was originally

---

frequencies of the subsets of T cells in Nadj, CP, PBMC, and PDAC samples. *F*, frequencies of the indicated PhenoGraph clusters of CD4$^+$ (*left panel*) and CD8$^+$ (*right panel*) T cells in Nadj, CP, PBMC, and PDAC samples. *E* and *F*, boxplot center lines = median, lower bound = 25% quantile, upper bound = 75% quantile, lower whisker = the smallest observation greater than or equal to the lower hinge − 1.5 × interquartile range (IQR), and upper whisker = the largest observation less than or equal to the upper hinge + 1.5 × IQR. Wilcoxon rank-sum test was used for statistical analysis (*$p < 0.05$, **$p < 0.01$, ***$p < 0.001$). Statistical analysis was not performed on Nadj samples. See also supplemental Fig. S4. CP, chronic pancreatitis; DN, double negative; Nadj, normal adjacent tissue; PBMC, peripheral blood mononuclear cell; PDAC, pancreatic ductal adenocarcinoma; TIL, tumor infiltrating lymphocyte; TME, tumor microenvironment; tSNE, t-distributed stochastic neighbor embedding.
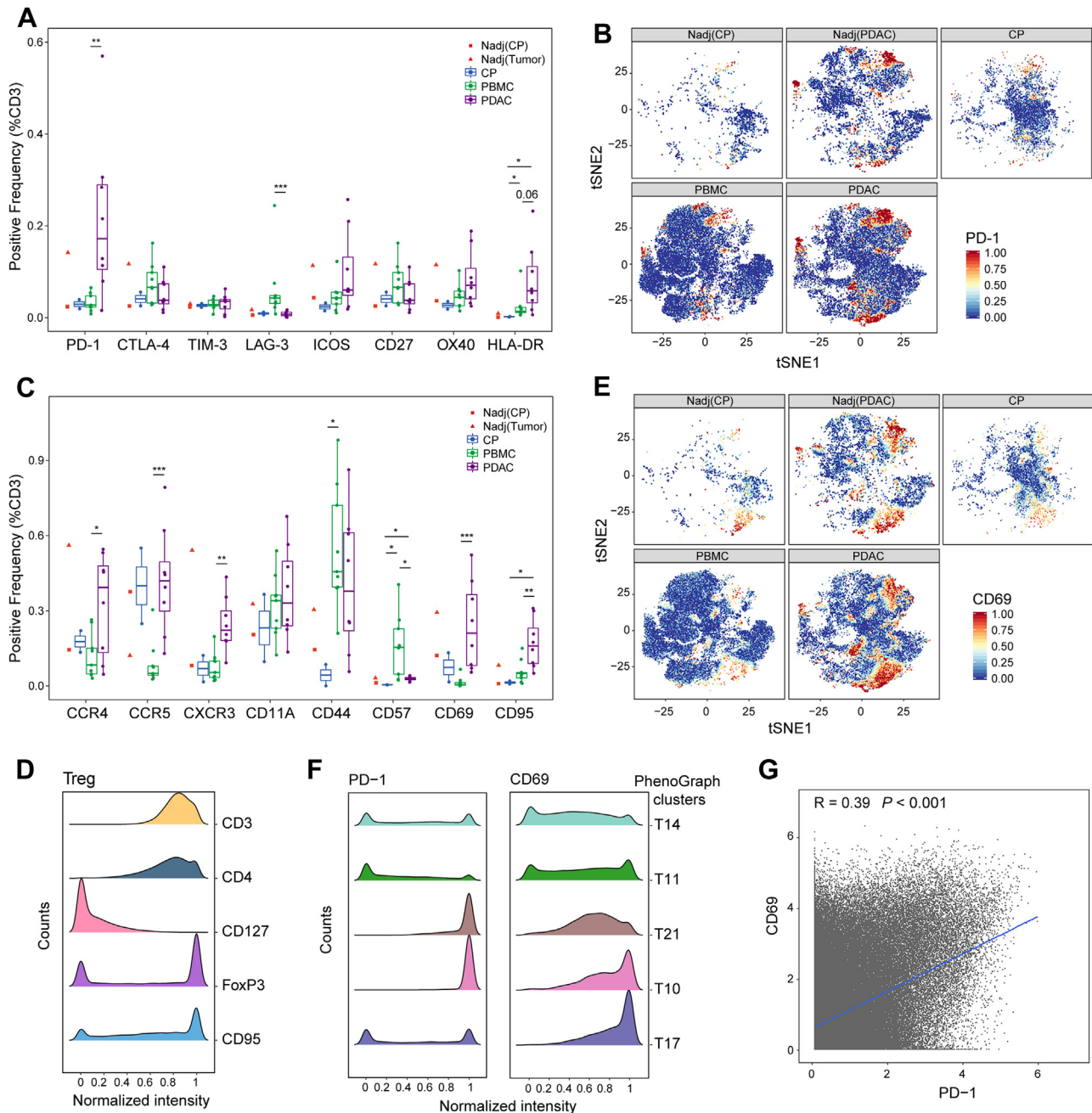
FIG. 4. **The expression of functional markers on PDAC-infiltrating T cells.** *A*, box plots displaying the percentage of immune checkpoint molecules in the T cells from Nadj, CP, PBMC, and PDAC samples. *B*, tSNE plots showing the expression of PD-1 in T cells. *C*, box plots displaying the percentage of other functional markers in the T cells. For *A* and *C*, boxplot center lines = median, lower bound = 25% quantile, upper bound = 75% quantile, lower whisker = the smallest observation greater than or equal to the lower hinge – 1.5 × interquartile range (IQR), and upper whisker = the largest observation less than or equal to the upper hinge + 1.5 × IQR. Wilcoxon rank-sum test was used for statistical analysis (*p < 0.05, **p < 0.01, ***p < 0.001). *D*, histograms displaying the expression of indicated markers on Treg cells. *E*, tSNE plots showing the expression of CD69 in T cells. *F*, histograms showing the expression of PD-1 and CD69 on cells from the PD-1+ clusters. *G*, scatterplot showing the correlation between the expression of CD69 and PD-1 in PDAC-infiltrating T cells. The Pearson correlation coefficient and *p* value are indicated, and the *fitted line* is shown in *blue*. Statistical analysis was not performed on Nadj samples. See also supplemental Fig. S5. CP, chronic pancreatitis; Nadj, normal adjacent tissue; PBMC, peripheral blood mononuclear cell; PD-1, programmed cell death protein 1; PDAC, pancreatic ductal adenocarcinoma; Treg, regulatory T cell; tSNE, peripheral blood mononuclear cell.

designated as a marker for end-stage and senescent T cells (43), and increased numbers of $CD8^+CD57^+$ T cells were observed in the TME of several types of tumors (44). However, a recent study reported that some $CD8^+CD57^+$ T cells could ultimately differentiate into cells subset with high perforin and killing activity (45). Our results suggested that the roles of CD57 required further evaluation in PDAC.

In addition, the proportion of $CD95^+$ (apoptosis antigen 1) cells was significantly increased in PDAC tumors compared with PBMC and CP samples for both of the $CD4^+$ and $CD8^+$ T-cell compartments (Fig. 4C and supplemental Fig. S5, B and D). CD95 is the prototypic death receptor (29), and apoptosis of T cells induced by CD95/CD95L is an important mechanism for maintaining peripheral tolerance and the termination of an ongoing immune response (46, 47). Our results suggest that CD95-mediated apoptosis of T cells may contribute to the immunosuppressive environment of PDAC. Meanwhile, Tregs, which were upregulated in PDAC, expressed high levels of CD95 (Fig. 4D). Weiss et al. (48) reported that Tregs resisted CD95-mediated apoptosis by FoxP3-mediated suppression of CD95L expression, and our data suggested that similar mechanism may also exist in PDAC.

Moreover, $CD69^+$ cells accounted for 24% of PDAC-infiltrating T cells, which was considerably increased compared with PBMCs, and the extensive expression of CD69 was observed in both $CD4^+$ and $CD8^+$ T-cell compartments (Fig. 4, C and E and supplemental Fig. S5B). CD69 is commonly used as a marker for T-cell activation (49) and is elevated in TME as a direct HIF-1α target gene induced by hypoxia (50). CD69 was recently associated with the exhaustion of tumor-infiltrating T cells (51). Interestingly, we observed that CD69 was coexpressed with PD-1 in clusters T14, T11, T21, T10, and T17 (Fig. 4F). The expression of these two molecules positively correlated with each other in PDAC-infiltrating T cells with a correlation coefficient of 0.39 (Fig. 4G). The results suggested that CD69 may be involved in PDAC-infiltrating T-cell exhaustion.

Our data revealed PD-1 as the most highly expressed immune checkpoint molecule in the TME of PDAC. To further explore the regulatory mechanisms associated with PD-1, we studied its correlation with all the examined immune markers at the single-cell level. The expression of the majority of the functional markers was elevated in $PD-1^+$ cells, including chemokine receptors CXCR3, CCR4, and CCR5; adhesion molecules CD11A and CD44; costimulatory immune checkpoint molecules OX40 and ICOS; coinhibitory immune checkpoint molecule CTLA-4; T-cell activation markers HLA-DR, CD69, and CD45RO; T-cell exhaustion marker CD57; death receptor CD95; and cytokines interleukin-17A and transforming growth factor beta (Fig. 5 and supplemental Fig. S6). The results suggested a complex and intertwined coordination between different immune regulatory mechanisms in $PD-1^+$ T cells. Finally, CCR7 and CD127, markers for naïve T cells, were the only two markers that exhibited significantly decreased expression in $PD-1^+$ cells (Fig. 5).

The Transcriptomic Immune Characteristics of PDAC

As described previously, IHC staining showed significant variability in the levels of T-cell infiltration among PDAC patients, with some tumors exhibiting sparse T-cell staining and some tumors showing relatively high T-cell density. The following single-cell analysis by mass cytometry further revealed the cellular composition diversity of the PDAC-filtrating immune cells. To better probe the immune landscape of PDAC and its correlation with other components of the TME in a larger sample set, we analyzed the RNA sequencing data of 146 PDAC bulk samples from TCGA (https://gdc.cancer.gov/).

First, correlation analysis showed that the majority of the investigated immune markers were coexpressed with PD-1 at the transcript level, such as CD11A, CD69, CTLA-4, and ICOS (Fig. 6A and supplemental Fig. S7A). Although several previous studies have utilized TCGA data for molecular subtyping of PDAC (52–54), the clinical implication of the combination of PD-1 and CD8 expression has not been investigated. Here, we stratified the PDAC samples from TCGA based on their immune scores predicted by ESTIMATE (55) and then defined three immune-based PDAC subtypes, including S1 ($CD8^+PD-1^+$ immune, n = 61), S2 ($CD8^{low}PD-1^{low}$ immune, n = 41), and S3 (immune desert, n = 44). CD8 and PD-1 were both expressed in S1, and their expression decreased in the order of S1, S2, to S3 (Fig. 6B). Other immune markers that were coexpressed with PD-1 as demonstrated by both mass cytometry analyses and transcriptomics, such as CD11A, CD69, CTLA-4, and ICOS, exhibited a similar trend (Fig. 6B).

Furthermore, GSVA indicated that S1 was markedly enriched in immune-related pathways, such as CTL, T helper, CTLA-4, and PD-1 signaling (Fig. 6, C and D and supplemental Table S6). Immune-related gene products, such as granzyme B (GZMB) and perforin-1 (PRF1), were significantly more abundant in S1 (Fig. 6D). Survival analysis showed that S1 patients with high expression of CD8 and PD-1 exhibited better prognosis compared with the other two subgroups (Fig. 6E and supplemental Table S7). In addition, the S2 subtype exhibited reduced immune cell infiltration compared with S1, especially for the T cell–related pathways (Fig. 6, C and D). However, medium-level enrichment in monocyte- and B cell–related pathways was observed for S2 (Fig. 6, C and D). Intriguingly, S2 was highly enriched in ECM-related pathways, such as collagen formation, collagen degradation, syndecan interactions, and cell–ECM interactions, suggesting a more active desmoplastic reaction in this subtype. The data indicated that the relatively lower immune infiltration in S2 compared with S1 may be caused by ECM exclusion.
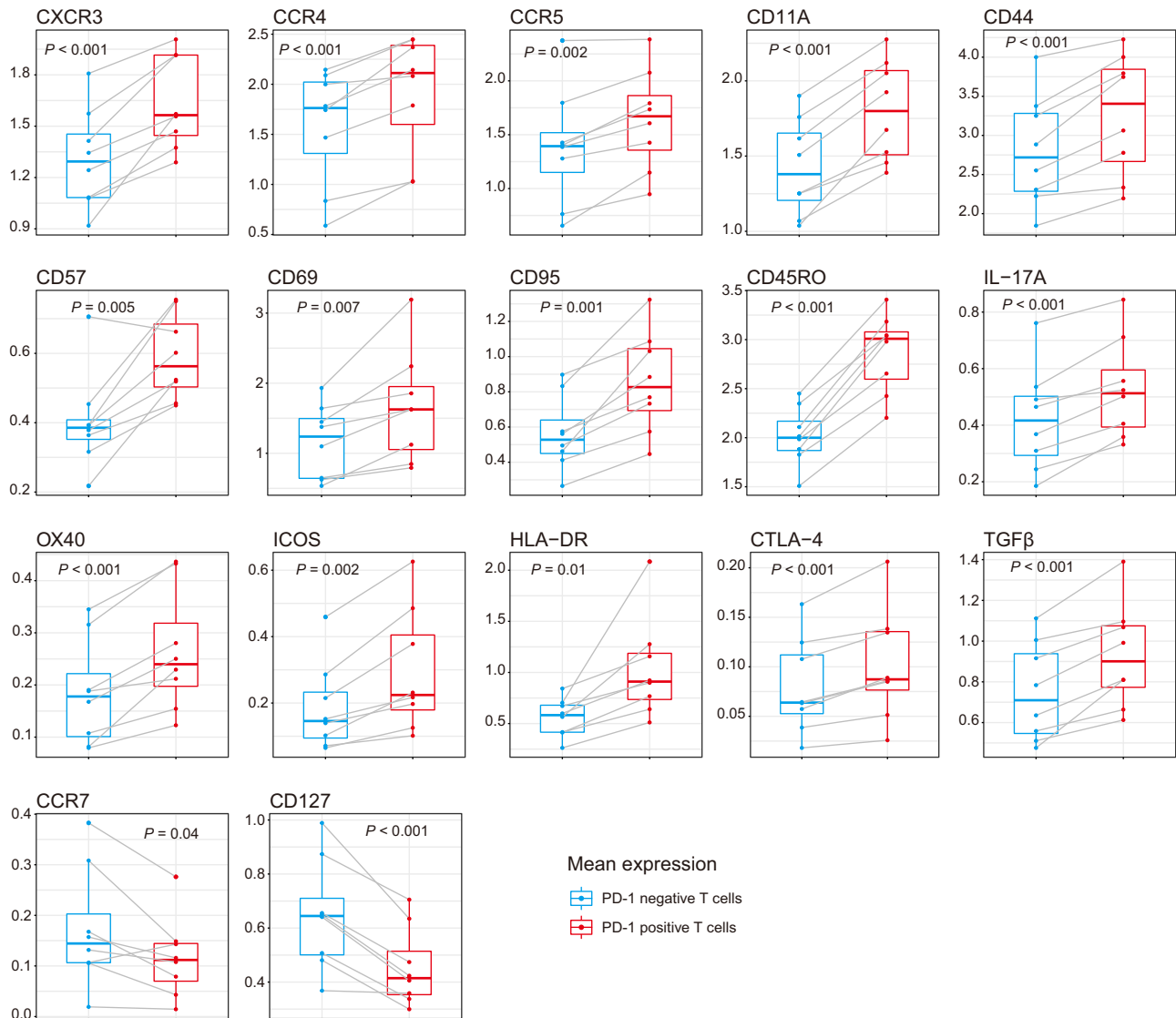
Fig. 5. **The distinct expression of functional markers between PD-1 positive and negative T cells.** Boxplot center lines = median, lower bound = 25% quantile, upper bound = 75% quantile, lower whisker = the smallest observation greater than or equal to the lower hinge − 1.5 × interquartile range (IQR), and upper whisker = the largest observation less than or equal to the upper hinge + 1.5 × IQR. Paired Student's *t* test was used for statistical analysis, and the *p* value is shown in the graph for each comparison. See also supplemental Fig. S6. PD-1, programmed cell death protein 1.

Moreover, around 30% of the PDAC tumors from TCGA database designated as subtype S3 showed the lowest level of immune infiltration, and this "immune desert" phenotype was also observed in some of our samples by IHC staining (supplemental Fig. S1*A*). The S3 samples exhibited both low levels of ECM and immune infiltration, suggesting that the low immune infiltration in these patients may not be caused by desmoplasia. In addition, we calculated the mutational load for the three subtypes of PDAC using the nonsynonymous mutation counts (supplemental Fig. S7*B*), and the results showed that the S2 and S3 samples exhibited higher mutational loads compared with S1 samples, which was opposite to the widely

accepted concept that large mutational burdens generate neoantigens for T-cell recognition and subsequently lead to increased recruitment of CTL (56). McGrail *et al.* (57) recently proposed that the DNA damage response protein ATM may be responsible for the immune filtration in the cancers driven by recurrent copy number alterations instead of recurrent mutations, such as pancreatic cancer. Indeed, we found that S2 and S3 samples exhibited reduced ATM expression levels compared with S1 samples (supplemental Fig. S7*C*). This observation may explain the paucity of immune cells in S3 samples. Moreover, S3 samples were highly enriched in proliferation-related pathways, such as cell cycle checkpoints,
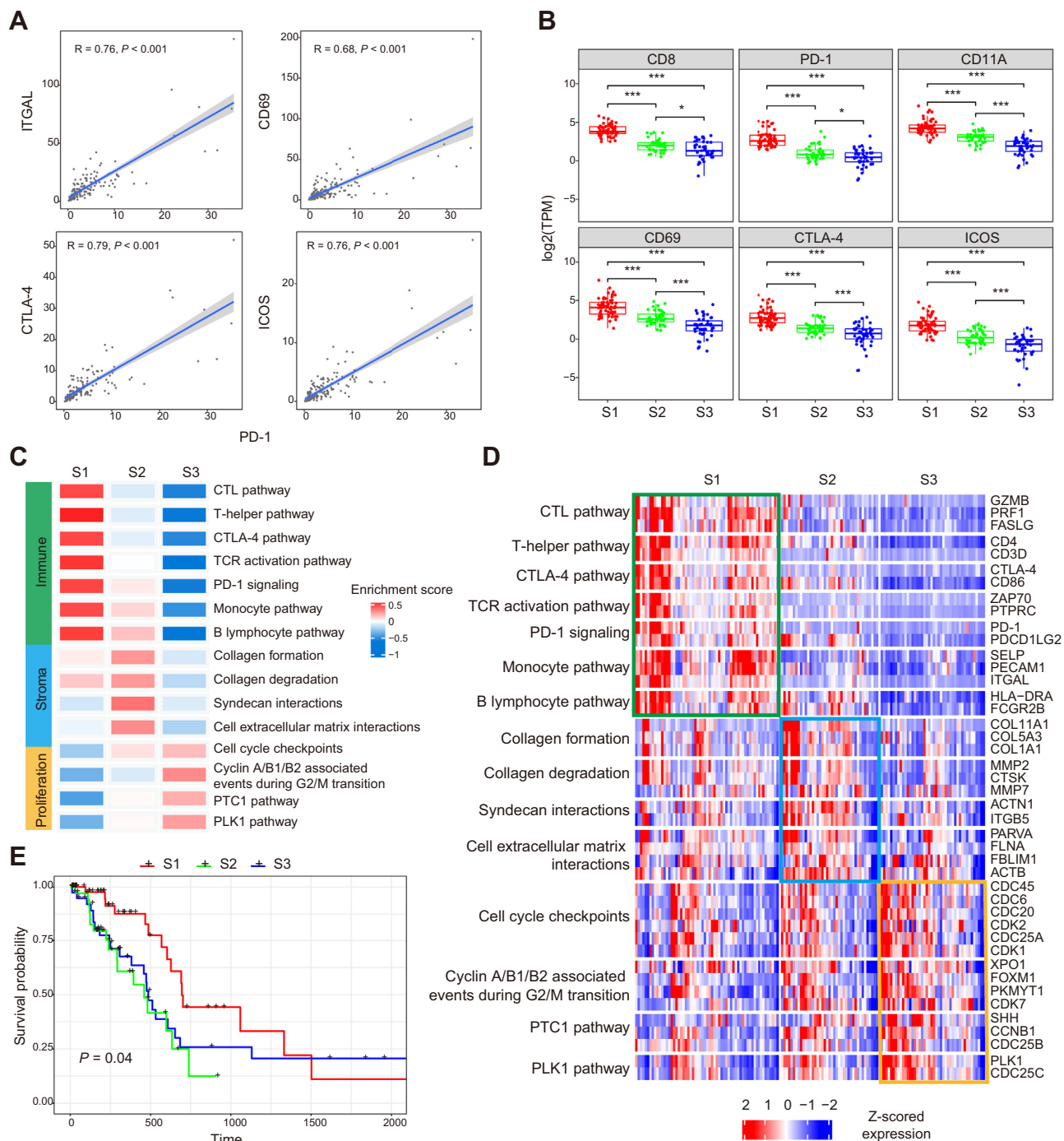
FIG. 6. **Transcriptomic immune subtyping of TCGA PDAC samples.** *A*, scatterplots showing the correlation between the RNA level of PD-1 and indicated immune-related genes across TCGA PDAC samples. Spearman correlations and *p* values are indicated, and the *fitted lines* are shown as *blue lines*. *B*, box plots showing the RNA expression of indicated genes in S1, S2, and S3 subtypes of TCGA PDAC samples. Boxplot center lines = median, lower bound = 25% quantile, upper bound = 75% quantile, lower whisker = the smallest observation greater than or equal to the lower hinge – 1.5 × interquartile range (IQR), and upper whisker = the largest observation less than or equal to the upper hinge + 1.5 × IQR. Wilcoxon rank-sum test was used for statistical analysis (*$p < 0.05$, **$p < 0.01$, ***$p < 0.001$). *C*, heatmap of the enrichment of the indicated pathways in the three subtypes. Colors represent the average GSVA enrichment scores. *D*, heatmap showing the expression of selected genes from the corresponding pathways with differential GSVA enrichment scores across subtypes. *E*, Kaplan–Meier curves of overall survival (OS) for each subtype of the TCGA PDAC patients, and *p* values are calculated using the log-rank test. RNA sequencing data and clinical information were obtained from TCGA (https://gdc.cancer.gov/) using the TCGAbiolinks (version: 2.16.0) R/Bioconductor package. See also supplemental Fig. S7 and supplemental Tables S6 and S7. GSVA, Gene set variation analysis; PD-1, programmed cell death protein 1; PDAC, pancreatic ductal adenocarcinoma; TCGA, The Cancer Genome Atlas; TPM, transcript per million.

cyclin A/B1/B2-associated events during G2/M transitions, PTC1 (protein patched homolog 1) pathway, and PLK1 (serine/threonine-protein kinase PLK1) pathway, whereas immune- and stroma-related genes were significantly inhibited in S3 samples compared with the other two subtypes (Fig. 6, C and D). Cell cycle–regulated genes, such as CDK1 and CDC25A, were highly expressed in S3 samples, and treatments targeting these molecules may provide therapeutic benefits for the S3 patients. Taken together, the data showed the diversity of the immune landscape in PDAC patients and revealed potential drug targets for patients in different subgroups.

Altogether, the results suggest that a subset of PDAC patients with relatively high abundance of PD-1$^+$CD8$^+$ T cells have better prognosis, and different mechanisms may exist for tumors with low immune cell infiltration. Moreover, the molecule-subtyping method presented here may provide valuable insights for prognosis and the design of personalized treatment strategies for individual PDAC patients with different molecular features.

DISCUSSION

Immune cells in the TME play important roles in regulating tumorigenesis and tumor progression (58). With the success of immune checkpoint blockade in various cancers, immune cells, especially T cells, have become the focus of anticancer immunotherapy development. To better understand the composition of PDAC-infiltrating immune cells, we performed single-cell mass cytometry analyses on different types of pancreatic samples, and the results revealed heterogeneous subsets of immune cells in the TME of PDAC, providing insights into the immune contexture of PDAC. By analyzing TCGA data from a larger cohort of patients, we observed tremendous interpatient heterogeneity of the immune landscape in PDAC tumors. The results further highlighted the needs for more sophisticated strategies to select potential responders to immunotherapy and personalized treatment approaches to improve the efficacy.

Our data suggested T cells as the dominant immune cell population in PDAC TME with significant viability among patients. We observed decreasing number of T cells from the Tm to Tns, and few T cells were observed in four tumor samples that could be considered as "cold tumor." We detected low levels of several inhibitory checkpoints, such as CTLA-4, TIM-3, and LAG-3, in PDAC-infiltrating T cells, suggesting that immunotherapies targeting these molecules might be unlikely to gain success. On the other hand, PD-1 was broadly expressed in PDAC-infiltrating T cells, including both CD8$^+$ and CD4$^+$ compartments. Expression of PD-1 is induced by T-cell receptor signaling and sustained upon chronic activation, leading to impaired T-cell functions and immunosuppression (59). Nevertheless, studies have also established PD-1 as a marker for functional avidity and antitumor

reactivity of antigen-specific T cells (39). This dual role of PD-1 was further confirmed here by the observed coexpression of both stimulatory and inhibitory molecules with PD-1. In addition, the frequencies of PD-1$^+$ cells markedly varied among patients, and RNA sequencing data from TCGA also revealed great interpatient heterogeneity of PD-1 expression. The better survival of TCGA patients with higher CD8 and PD-1 expression indicated PD-1 as a putative marker for antitumor immune response. Furthermore, as shown by IHC staining, although relatively high density of T cells was observed in some tumors, they were largely excluded from the Tn. Therefore, a combination of PD-1 blockade and therapies targeting stromal elements may be beneficial to improve patient outcome. The combination of PD-1 and focal adhesion kinase-1 inhibitors is currently being evaluated in several clinical trials, for example, NCT02758587 and NCT03727880.

Intriguingly, the mass cytometry data showed that several costimulatory molecules were expressed in PDAC-infiltrating immune cells at relatively higher frequencies compared with the other samples. For example, we observed a subset of MPs expressing CD137L in PDAC samples. The CD137–CD137L interaction enhances type 1 cell-mediated immune responses, and the reverse CD137L signal promotes the survival and proliferation of proinflammatory monocytes and stimulates their migration and extravasation into tissues (33). CD137 agonists exhibit antitumor activity in multiple cancer types (32, 33). In addition, transgenic CD137L expression induces cytotoxic T-cell expansion and inhibits tumor growth and metastasis (59). Substantial evidence has shown that targeting CD137/CD137L synergizes with cancer vaccines and immune checkpoint inhibitors in boosting anticancer immune responses (59). Moreover, a recent study reported that agonistic CD137 monoclonal antibody increased CTL growth in PDAC tumors (60, 61). Here, our data further revealed the possibility of targeting the CD137–CD137L interaction for PDAC treatment. It would be interesting to explore the impact of CD137 agonists on the proinflammatory activity of the antigen-presenting cells as well as its effect in combination with PD-1/programmed cell death receptor ligand 1 checkpoint inhibitors.

Another interesting observation is the extensive expression of CD69 in PDAC-infiltrating T cells with a mean frequency of 24%. The best-known function of CD69 is the regulation of local retention of lymphocytes through the interaction with sphingosine-1-phospate receptor 1 (62). CD69 is also a marker of tissue-resident memory T cells, a subpopulation of memory CD8$^+$ T cells that persist in peripheral tissues (63). Several studies have shown that CD69 knockout or administration of anti-CD69 monoclonal antibodies resulted in the augmentation of antitumor responses (64, 65). However, whether CD69 delivers intracellular signaling to regulate T-cell activities is still unclear, and its specific roles in PDAC remain unknown. Here, we observed a significantly higher level of CD69 in PDAC-infiltrating CD8$^+$ T cells compared with those

in blood or CP tissues (supplemental Fig. S5B). Moreover, CD69 was coexpressed with PD-1 at the single-cell level in several T-cell subsets (Fig. 4, F and G), which was consistent with a recent report that CD69-deficient tumor-infiltrating CD8$^+$ T cells exhibited a less exhausted phenotype than CD69-sufficient tumor-infiltrating CD8$^+$ T cells (51). Our data implied an intrinsic correlation between CD69 and PD-1 and suggested the potential clinical application of targeting CD69 to further invigorate exhausted T cells in the microenvironment of PDAC.

In recent years, many large-scale proteomic studies of PDAC have been reported, providing valuable opportunities to identify useful biomarkers for diagnosis and potential therapeutic targets for treatment (66–68). However, the proteome data derived from bulk tissues are often insufficient to resolve the detailed immune components in the TME. Our single-cell data complement the large-scale proteomic data in several aspects. First, although thousands of proteins can be detected by proteomics, many classical immune markers are not detectable or only detected in a small fraction of samples. Protein marker expression at the single-cell level was examined in this study, allowing the characterization of well-defined immune cell populations and the identification of disease-associated immune phenotypes. Furthermore, unlike proteomic studies focusing on the analysis of global protein expression changes, we investigated well-characterized markers, such as immune checkpoints, which are direct targets of immunotherapies but are often missing in global proteomic studies. For example, Le Large et al. (67) performed proteomic analysis on laser-capture microdissected and bulk PDAC samples (n = 16) and identified over 6000 proteins. However, none of the eight checkpoint molecules we examined here were detected. More recently, Cao et al. (68) reported a proteogenomic study of PDAC with the largest sample size (n = 140) and deepest coverage (11,662 proteins and 51,469 phosphosites) for the PDAC proteome up to date. In this study, TIM-3 and ICOS were detected in 50% and 20% of their samples at the protein level, whereas the other checkpoint molecules, that is, PD-1, CTLA-4, CD27, OX40, and CD137L, were not observed. Interestingly, the authors also detected phosphorylation sites on LAG-3, PD-1, and TIM-3 from 11%, 80%, and 40% of the samples, providing additional information regarding the activities of these molecules. Nevertheless, it is still challenging for proteomics to analyze immune checkpoints, possibly because they are all membrane proteins with low abundance. To integrate single-cell mass cytometry and global proteome analysis may provide a new opportunity to better understand the immune microenvironment in cancer.

Meanwhile, this study has limitations. Compared with single-cell transcriptomics that has been employed to reveal valuable information regarding the immune microenvironment in various cancers in the recent years (69, 70), much fewer markers were investigated in this study. However, mass cytometry measures protein expression features, which are more directly associated with cell phenotype than transcripts.

In addition, we were only able to obtain mass cytometry data from eight PDAC tumors in this study, and few immune cells were obtained from four of 12 investigated samples; therefore, the observations may only apply to the immune-enriched subtype of PDAC. A larger patient cohort is required to achieve a higher level of statistical power and to associate the identified cell phenotypes with clinical outcome. Moreover, the biological functions and clinical implications of some identified phenotypes need to be further evaluated.

In conclusion, our data reveal a single-cell atlas of the tumor-infiltrating immune cells in PDAC, especially focusing on the cellular and functional composition of the T-cell compartment. The results provide clinically relevant information regarding useful cell phenotypes and biomarkers with potential impact on the optimization of immunotherapies for PDAC.

Author contributions—R. C. conceptualization; H. W. methodology; H. W., L. C., L. Q., and N. J. investigation; L. C., Z. Z., H. G., T. S., J. L., and H. L. resources; H. W. writing–original draft; R. C. writing–review & editing; N. Z. and R. C. supervision; N. Z. and R. C. project administration.

Conflict of interest—The authors declare no competing interests.

Abbreviations—The abbreviations used are: Ab, antibody; CCR5, CC chemokine receptor 5; CP, chronic pancreatitis; CTLA-4, cytotoxic T lymphocyte–associated protein 4; ECM,

extracellular matrix; EM, effector memory; FoxP3, forkhead box P3; GSVA, gene set variation analysis; ICOS, inducible T-cell costimulatory; IHC, immunohistochemistry; LAG-3, lymphocyte-activation gene 3; MP, mononuclear phagocyte; Nadj, normal adjacent; OX40, tumor necrosis factor receptor superfamily member 4; PBMC, peripheral blood mononuclear cell; PD-1, programmed cell death protein 1; PDAC, pancreatic ductal adenocarcinoma; TCGA, The Cancer Genome Atlas; TIM-3, T-cell immunoglobulin and mucin-domain containing-3; Tm, tumor margin; TME, tumor microenvironment; Tn, tumor nest; Treg, regulatory T cell; tSNE, t-distributed stochastic neighbor embedding.

REFERENCES

1. Kleeff, J., Korc, M., Apte, M., La Vecchia, C., Johnson, C. D., Biankin, A. V., *et al*. (2016) Pancreatic cancer. *Nat. Rev. Dis. Primers* **2**, 16022
2. Rahib, L., Smith, B. D., Aizenberg, R., Rosenzweig, A. B., Fleshman, J. M., and Matrisian, L. M. (2014) Projecting cancer incidence and deaths to 2030: the unexpected burden of thyroid, liver, and pancreas cancers in the United States. *Cancer Res.* **74**, 2913–2921
3. Bailey, P., Chang, D. K., Nones, K., Johns, A. L., Patch, A. M., Gingras, M. C., *et al*. (2016) Genomic analyses identify molecular subtypes of pancreatic cancer. *Nature* **531**, 47–52
4. Cancer Genome Atlas Research Network. (2017) Integrated genomic characterization of pancreatic ductal adenocarcinoma. *Cancer Cell* **32**, 185–203.e13
5. Moffitt, R. A., Marayati, R., Flate, E. L., Volmar, K. E., Loeza, S. G., Hoadley, K. A., *et al*. (2015) Virtual microdissection identifies distinct tumor- and stroma-specific subtypes of pancreatic ductal adenocarcinoma. *Nat. Genet.* **47**, 1168–1178
6. Makohon-Moore, A., and Iacobuzio-Donahue, C. A. (2016) Pancreatic cancer biology and genetics from an evolutionary perspective. *Nat. Rev. Cancer* **16**, 553–565
7. Iacobuzio-Donahue, C. A., Ryu, B., Hruban, R. H., and Kern, S. E. (2002) Exploring the host desmoplastic response to pancreatic carcinoma – gene expression of stromal and neoplastic cells at the site of primary invasion. *Am. J. Pathol.* **160**, 91–99
8. Ene-Obong, A., Clear, A. J., Watt, J., Wang, J., Fatah, R., Riches, J. C., *et al*. (2013) Activated pancreatic stellate cells sequester CD8+ T cells to reduce their infiltration of the juxtatumoral compartment of pancreatic ductal adenocarcinoma. *Gastroenterology* **145**, 1121–1132
9. Feig, C., Jones, J. O., Kraman, M., Wells, R. J., Deonarine, A., Chan, D. S., *et al*. (2013) Targeting CXCL12 from FAP-expressing carcinoma-associated fibroblasts synergizes with anti-PD-L1 immunotherapy in pancreatic cancer. *Proc. Natl. Acad. Sci. U. S. A.* **110**, 20212–20217
10. Carstens, J. L., Correa, D. S. P., Yang, D., Barua, S., Wang, H., Rao, A., *et al*. (2017) Spatial computation of intratumoral T cells correlates with survival of patients with pancreatic cancer. *Nat. Commun.* **8**, 15095
11. Shibuya, K. C., Goel, V. K., Xiong, W., Sham, J. G., Pollack, S. M., Leahy, A. M., *et al*. (2014) Pancreatic ductal adenocarcinoma contains an effector and regulatory immune cell infiltrate that is altered by multimodal neoadjuvant treatment. *PLoS One* **9**, e96565
12. Daley, D., Zambirinis, C. P., Seifert, L., Akkad, N., Mohan, N., Werba, G., *et al*. (2016) Gammadelta T cells support pancreatic oncogenesis by restraining alphabeta T cell activation. *Cell* **166**, 1485–1499.e15
13. Stromnes, I. M., Hulbert, A., Pierce, R. H., Greenberg, P. D., and Hingorani, S. R. (2017) T-cell localization, activation, and clonal expansion in human pancreatic ductal adenocarcinoma. *Cancer Immunol. Res.* **5**, 978–991
14. Jang, J. E., Hajdu, C. H., Liot, C., Miller, G., Dustin, M. L., and Bar-Sagi, D. (2017) Crosstalk between regulatory T cells and tumor-associated dendritic cells negates anti-tumor immunity in pancreatic cancer. *Cell Rep.* **20**, 558–571
15. Vonderheide, R. H., and Bayne, L. J. (2013) Inflammatory networks and immune surveillance of pancreatic carcinoma. *Curr. Opin. Immunol.* **25**, 200–205

16. Beatty, G. L., Chiorean, E. G., Fishman, M. P., Saboury, B., Teitelbaum, U. R., Sun, W., *et al*. (2011) CD40 agonists alter tumor stroma and show efficacy against pancreatic carcinoma in mice and humans. *Science* **331**, 1612–1616
17. Larkin, J., Chiarion-Sileni, V., Gonzalez, R., Grob, J. J., Cowey, C. L., Lao, C. D., *et al*. (2015) Combined nivolumab and ipilimumab or monotherapy in untreated melanoma. *N. Engl. J. Med.* **373**, 23–34
18. Garon, E. B., Rizvi, N. A., Hui, R., Leighl, N., Balmanoukian, A. S., Eder, J. P., *et al*. (2015) Pembrolizumab for the treatment of non-small-cell lung cancer. *N. Engl. J. Med.* **372**, 2018–2028
19. Royal, R. E., Levy, C., Turner, K., Mathur, A., Hughes, M., Kammula, U. S., *et al*. (2010) Phase 2 trial of single agent ipilimumab (anti-CTLA-4) for locally advanced or metastatic pancreatic adenocarcinoma. *J. Immunother.* **33**, 828–833
20. Brahmer, J. R., Tykodi, S. S., Chow, L. Q., Hwu, W. J., Topalian, S. L., Hwu, P., *et al*. (2012) Safety and activity of anti-PD-L1 antibody in patients with advanced cancer. *N. Engl. J. Med.* **366**, 2455–2465
21. Lawrence, M. S., Stojanov, P., Polak, P., Kryukov, G. V., Cibulskis, K., Sivachenko, A., *et al*. (2013) Mutational heterogeneity in cancer and the search for new cancer-associated genes. *Nature* **499**, 214–218
22. Wood, L. D., and Hruban, R. H. (2012) Pathology and molecular genetics of pancreatic neoplasms. *Cancer J.* **18**, 492–501
23. Feig, C., Gopinathan, A., Neesse, A., Chan, D. S., Cook, N., and Tuveson, D. A. (2012) The pancreas cancer microenvironment. *Clin. Cancer Res.* **18**, 4266–4276
24. Xue, R., Chen, L., Zhang, C., Fujita, M., Li, R., Yan, S. M., *et al*. (2019) Genomic and transcriptomic profiling of combined hepatocellular and intrahepatic cholangiocarcinoma reveals distinct molecular subtypes. *Cancer Cell* **35**, 932–947
25. Lavin, Y., Kobayashi, S., Leader, A., Amir, E. D., Elefant, N., Bigenwald, C., *et al*. (2017) Innate immune landscape in early lung adenocarcinoma by paired single-cell analyses. *Cell* **169**, 750–765.e17
26. Amir, E., Davis, K. L., Tadmor, M. D., Simonds, E. F., Levine, J. H., Bendall, S. C., *et al*. (2013) viSNE enables visualization of high dimensional single-cell data and reveals phenotypic heterogeneity of leukemia. *Nat. Biotechnol.* **31**, 545–552
27. van der Maaten, L., and Hinton, G. E. (2008) Visualizing data using t-SNE. *J. Mach. Learn. Res.* **9**, 2579–2605
28. Levine, J. H., Simonds, E. F., Bendall, S. C., Davis, K. L., Amir, E., Tadmor, M. D., *et al*. (2015) Data-driven phenotypic dissection of AML reveals progenitor-like cells that correlate with prognosis. *Cell* **162**, 184–197
29. Paulsen, M., and Janssen, O. (2011) Pro- and anti-apoptotic CD95 signaling in T cells. *Cell Commun. Signal.* **9**, 7
30. Nanki, T., Takada, K., Komano, Y., Morio, T., Kanegane, H., Nakajima, A., *et al*. (2009) Chemokine receptor expression and functional effects of chemokines on B cells: implication in the pathogenesis of rheumatoid arthritis. *Arthritis Res. Ther.* **11**, R149
31. Honczarenko, M., Le, Y., Glodek, A. M., Majka, M., Campbell, J. J., Ratajczak, M. Z., *et al*. (2002) CCR5-binding chemokines modulate CXCL12 (SDF-1)-induced responses of progenitor B cells in human bone marrow through heterologous desensitization of the CXCR4 chemokine receptor. *Blood* **100**, 2321–2329
32. Melero, I., Shuford, W. W., Newby, S. A., Aruffo, A., Ledbetter, J. A., Hellstrom, K. E., *et al*. (1997) Monoclonal antibodies against the 4-1BB T-cell activation molecule eradicate established tumors. *Nat. Med.* **3**, 682–685
33. Dharmadhikari, B., Wu, M., Abdullah, N. S., Rajendran, S., Ishak, N. D., Nickles, E., *et al*. (2016) CD137 and CD137L signals are main drivers of type 1, cell-mediated immune responses. *Oncoimmunology* **5**, e1113367
34. Idorn, M., and Thor, S. P. (2018) Chemokine receptors and exercise to tackle the inadequacy of T cell homing to the tumor site. *Cells* **7**, 108
35. Slaney, C. Y., Kershaw, M. H., and Darcy, P. K. (2014) Trafficking of T cells into tumors. *Cancer Res.* **74**, 7168–7174
36. Chevrier, S., Levine, J. H., Zanotelli, V., Silina, K., Schulz, D., Bacac, M., *et al*. (2017) An immune atlas of clear cell renal cell carcinoma. *Cell* **169**, 736–749.e18
37. Wagner, J., Rapsomaniki, M. A., Chevrier, S., Anzeneder, T., Langwieder, C., Dykgers, A., *et al*. (2019) A single-cell atlas of the tumor and immune ecosystem of human breast cancer. *Cell* **177**, 1330–1345.e18
38. van der Leun, A. M., Thommen, D. S., and Schumacher, T. N. (2020) CD8(+) T cell states in human cancer: insights from single-cell analysis. *Nat. Rev. Cancer* **20**, 218–232

39. Simon, S., and Labarriere, N. (2017) PD-1 expression on tumor-specific T cells: friend or foe for immunotherapy? *Oncoimmunology* **7**, e1364828

40. Badoual, C., Hans, S., Merillon, N., Van Ryswick, C., Ravel, P., Benhamouda, N., *et al*. (2013) PD-1-expressing tumor-infiltrating T cells are a favorable prognostic biomarker in HPV-associated head and neck cancer. *Cancer Res.* **73**, 128–138

41. Topalian, S. L., Drake, C. G., and Pardoll, D. M. (2015) Immune checkpoint blockade: a common denominator approach to cancer therapy. *Cancer Cell* **27**, 450–461

42. Saraiva, D. P., Jacinto, A., Borralho, P., Braga, S., and Cabral, M. G. (2018) HLA-DR in cytotoxic T lymphocytes predicts breast cancer patients' response to neoadjuvant chemotherapy. *Front. Immunol.* **9**, 2605

43. Abo, T., and Balch, C. M. (1981) A differentiation antigen of human NK and K cells identified by a monoclonal antibody (HNK-1). *J. Immunol.* **127**, 1024–1029

44. Strioga, M., Pasukoniene, V., and Characiejus, D. (2011) CD8+ CD28- and CD8+ CD57+ T cells and their role in health and disease. *Immunology* **134**, 17–32

45. Wu, R. C., Hwu, P., and Radvanyi, L. G. (2012) New insights on the role of CD8(+)CD57(+) T-cells in cancer. *Oncoimmunology* **1**, 954–956

46. Li-Weber, M., and Krammer, P. H. (2002) The death of a T-cell: expression of the CD95 ligand. *Cell Death Differ.* **9**, 101–103

47. Krammer, P. H. (2000) CD95's deadly mission in the immune system. *Nature* **407**, 789–795

48. Weiss, E. M., Schmidt, A., Vobis, D., Garbi, N., Lahl, K., Mayer, C. T., *et al*. (2011) Foxp3-mediated suppression of CD95L expression confers resistance to activation-induced cell death in regulatory T cells. *J. Immunol.* **187**, 1684–1691

49. Cibrian, D., and Sanchez-Madrid, F. (2017) CD69: from activation marker to metabolic gatekeeper. *Eur. J. Immunol.* **47**, 946–953

50. Labiano, S., Melendez-Rodriguez, F., Palazon, A., Teijeira, A., Garasa, S., Etxeberria, I., *et al*. (2017) CD69 is a direct HIF-1alpha target gene in hypoxia as a mechanism enhancing expression on tumor-infiltrating T lymphocytes. *Oncoimmunology* **6**, e1283468

51. Mita, Y., Kimura, M. Y., Hayashizaki, K., Koyama-Nasu, R., Ito, T., Motohashi, S., *et al*. (2018) Crucial role of CD69 in anti-tumor immunity through regulating the exhaustion of tumor-infiltrating T cells. *Int. Immunol.* **30**, 559–567

52. Balli, D., Rech, A. J., Stanger, B. Z., and Vonderheide, R. H. (2017) Immune cytolytic activity stratifies molecular subsets of human pancreatic cancer. *Clin. Cancer Res.* **23**, 3129–3138

53. Zhao, L., Zhao, H., and Yan, H. (2018) Gene expression profiling of 1200 pancreatic ductal adenocarcinoma reveals novel subtypes. *BMC Cancer* **18**, 603

54. Kandimalla, R., Tomihara, H., Banwait, J. K., Yamamura, K., Singh, G., Baba, H., *et al*. (2020) A 15-gene immune, stromal, and proliferation gene signature that significantly associates with poor survival in patients with pancreatic ductal adenocarcinoma. *Clin. Cancer Res.* **26**, 3641–3648

55. Yoshihara, K., Shahmoradgoli, M., Martinez, E., Vegesna, R., Kim, H., Torres-Garcia, W., *et al*. (2013) Inferring tumour purity and stromal and immune cell admixture from expression data. *Nat. Commun.* **4**, 2612

56. Charoentong, P., Finotello, F., Angelova, M., Mayer, C., Efremova, M., Rieder, D., *et al*. (2017) Pan-cancer immunogenomic analyses reveal genotype-immunophenotype relationships and predictors of response to checkpoint blockade. *Cell Rep.* **18**, 248–262

57. McGrail, D. J., Federico, L., Li, Y., Dai, H., Lu, Y., Mills, G. B., *et al*. (2018) Multi-omics analysis reveals neoantigen-independent immune cell infiltration in copy-number driven cancers. *Nat. Commun.* **9**, 1317

58. Quail, D. F., and Joyce, J. A. (2013) Microenvironmental regulation of tumor progression and metastasis. *Nat. Med.* **19**, 1423–1437

59. Sharpe, A. H., and Pauken, K. E. (2018) The diverse functions of the PD1 inhibitory pathway. *Nat. Rev. Immunol.* **18**, 153–167

60. Srivastava, A. K., Dinc, G., Sharma, R. K., Yolcu, E. S., Zhao, H., and Shirwan, H. (2014) SA-4-1BBL and monophosphoryl lipid A constitute an efficacious combination adjuvant for cancer vaccines. *Cancer Res.* **74**, 6441–6451

61. Sakellariou-Thompson, D., Forget, M. A., Creasy, C., Bernard, V., Zhao, L., Kim, Y. U., *et al*. (2017) 4-1BB agonist focuses CD8(+) tumor-infiltrating T-cell growth into a distinct repertoire capable of tumor recognition in pancreatic cancer. *Clin. Cancer Res.* **23**, 7263–7275

62. Shiow, L. R., Rosen, D. B., Brdickova, N., Xu, Y., An, J., Lanier, L. L., *et al*. (2006) CD69 acts downstream of interferon-alpha/beta to inhibit S1P1 and lymphocyte egress from lymphoid organs. *Nature* **440**, 540–544

63. Mami-Chouaib, F., Blanc, C., Corgnac, S., Hans, S., Malenica, I., Granier, C., *et al*. (2018) Resident memory T cells, critical components in tumor immunology. *J. Immunother. Cancer* **6**, 87

64. Esplugues, E., Sancho, D., Vega-Ramos, J., Martinez, C., Syrbe, U., Hamann, A., *et al*. (2003) Enhanced antitumor immunity in mice deficient in CD69. *J. Exp. Med.* **197**, 1093–1106

65. Esplugues, E., Vega-Ramos, J., Cartoixa, D., Vazquez, B. N., Salaet, I., Engel, P., *et al*. (2005) Induction of tumor NK-cell immunity by anti-CD69 antibody therapy. *Blood* **105**, 4399–4406

66. Meleady, P., Abdul Rahman, R., Henry, M., Moriarty, M., and Clynes, M. (2020) Proteomic analysis of pancreatic ductal adenocarcinoma. *Expert Rev. Proteomics* **17**, 453–467

67. Le Large, T. Y., Mantini, G., Meijer, L. L., Pham, T. V., Funel, N., van Grieken, N. C., *et al*. (2020) Microdissected pancreatic cancer proteomes reveal tumor heterogeneity and therapeutic targets. *JCI Insight* **5**, e138290

68. Cao, L., Huang, C., Zhou, D. C., Hu, Y., Lih, T. M., Savage, S. R., *et al*. (2021) Proteogenomic characterization of pancreatic ductal adenocarcinoma. *Cell* **184**, 5031–5052.e26

69. Zhang, Q., He, Y., Luo, N., Patel, S. J., Han, Y., Gao, R., *et al*. (2019) Landscape and dynamics of single immune cells in hepatocellular carcinoma. *Cell* **179**, 829–845

70. Zheng, C., Zheng, L., Yoo, J. K., Guo, H., Zhang, Y., Guo, X., *et al*. (2017) Landscape of infiltrating T cells in liver cancer revealed by single-cell sequencing. *Cell* **169**, 1342–1356